Supplementary Information for

Highly Efficient Heteronuclear Polarization Transfer by Dipolar-Echo Edited R-Symmetry Sequences in Solid-State NMR

Lixin Liang[1], Kuizhi Chen[1], Guangjin Hou[1*]

[1]*State Key Laboratory of Catalysis, National Laboratory for Clean Energy, 2011-Collaborative Innovation Center of Chemistry for Energy Materials, Dalian Institute of Chemical Physics, Chinese Academy of Sciences, Zhongshan Road 457, Dalian 116023, China.*

Corresponding author: ghou@dicp.ac.cn

Table of contents

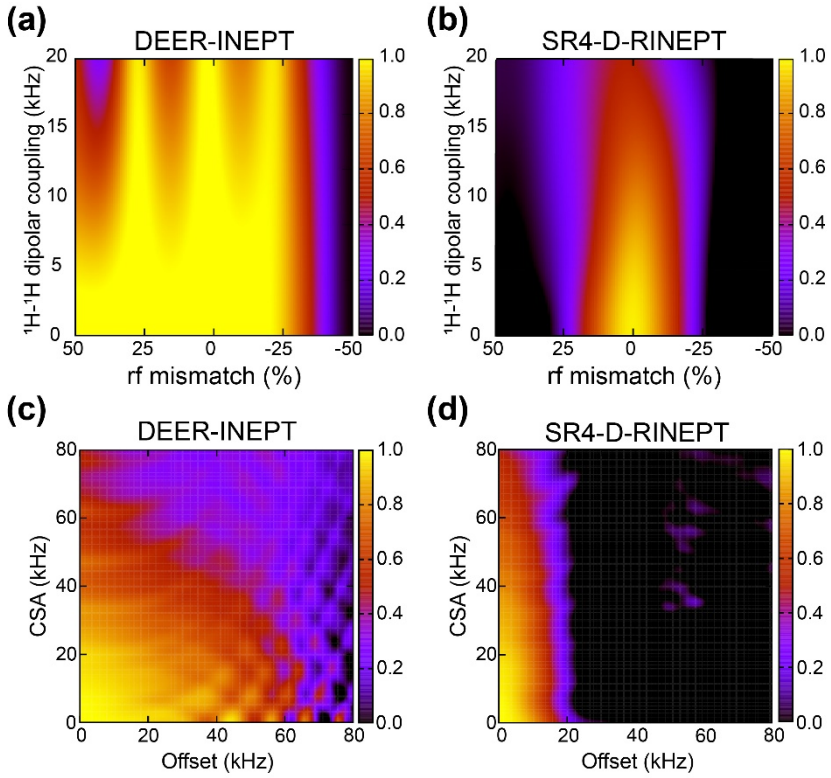

Figure S1. Simulated performances of (a)/(c) $^{1}H \rightarrow ^{15}N$ DEER-INEPT (f_w = 0) and (b)/(d) $^{1}H \rightarrow ^{13}C$ SR4-D-RINEPT methods, under the combined effects of (a)/(b) rf mismatch and ^{1}H-^{1}H dipolar coupling, as well as (c)/(d) resonance offset and ^{1}H CSA. The simulations use isolated $^{1}H \rightarrow ^{15}N$ spin pair, in 18.8 T magnetic field and 60 kHz MAS.

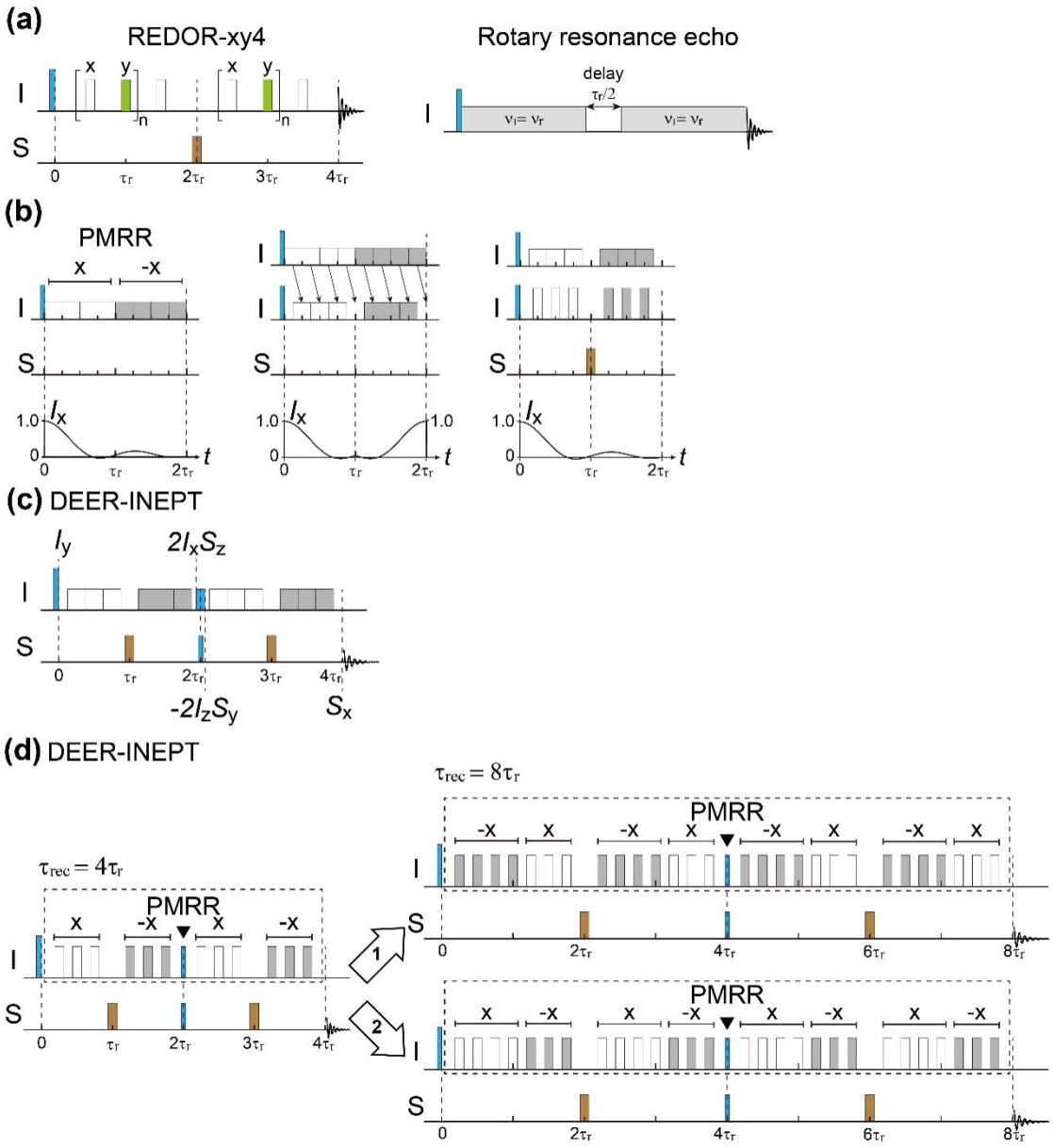

Figure S2. (a) The representative pulse sequences of REDOR-xy4 (left) and rotary resonance echo (right). (b) Construction of dipolar echo in PMRR dipolar recoupling sequence. The curves are the simulated intensities of I_x magnetization dephased by *I*-*S* dipolar coupling. The simulations use ideal pulses (with pulse duration $\tau_p \rightarrow 0$) in PMRR recoupling; (c) Illustration of the polarization transfer mechanism of DEER-INEPT (d) Two phase cycling scheme for DEER-INEPT pulse sequences as recoupling time increased. The phases of π pulses in PMRR are indicated as x/-x and by white/grey rectangles.

1. Theory

1.1 Dipolar Echo in PMRR sequence

The dipolar echo is inspired by REDOR (Rotational-Echo DOuble Resonance)[1] and rotary resonance echo[2,3], proposed by Gullion and Gan, respectively. The pulse sequences of both methods are illustrated in **Figure S2a**. The REDOR is famous for its accurate measurement of heteronuclear dipolar coupling constant, and the rotary resonance echo can also do the similar job. For REDOR pulse sequence, if one ignores the xy4 phase cycle and expand the durations of π pulses on *I* spin until the neighboring pulses touches each other, a rotary resonance echo will then be formed on *I* spin. The similarities of both methods come from their recoupling mechanism, i.e., rotary resonance recoupling (R^3).[4,5] The R^3 occurs under MAS condition where the heteronuclear dipolar coupling is averaged out by fast sample spinning. Under MAS condition and in a dislike I-S spin pair coupled through dipolar interaction, if the rf amplitude (ν_1) on *I* spin matches a multiple of the spinning frequency (ν_r), i.e., $\nu_1 = n\nu_r$ (n = 1, 2), the *I*-*S* dipolar interaction and also the *I* spin CSA are reintroduced by the rf irradiation.[4,5] The rotary resonance echo reveals that a central delay, with duration of half (or a quarter of) rotor cycle for n = 1 (or n = 2) matching condition, inverts the I spin magnetization, creating echo of *I* spin CSA.[2,3]

As a recently developed sequence for heteronuclear dipolar recoupling, PMRR relies on the n = 2 R^3 condition.[6] Therefore, similar to rotary resonance echo, an echo of I-S dipolar interaction can also be constructed during PMRR recoupling. However, different from the rotary resonance echo which has no phase modulation, the PMRR uses (x, $-x$) phase modulation for robust performance[6]. This phase modulation must be remained in the design of echo. For this purpose, a $\tau_r/4$ time shift is introduced to the PMRR which repetitive unit can be regarded as 8 × π pulses with (*xxxx*, *-x-x-x-x*) phase cycle, as shown by **Figure S2b** (left figure). After the time shift, the last pulse in PMRR is placed at the end of the last rotor cycle and thus can be omitted. Then, further removal of the central pulse can reverse the sign of recoupled *I* spin CSA and *I*-*S* dipolar

Hamiltonian. At the end of the last rotor cycle, an echo of the dipolar Hamiltonian is formed, as illustrated by the **Figure S2b** (middle figure). In order to select the *I*-*S* dipolar Hamiltonian, a π pulse is applied on *S* spin synchronized with the central delay of PMRR sequence, as shown in **Figure S2b** (right figure). As consequence, this echo is able to refocus the *I* spin CSA, as well as *I* and *S* spin chemical shift. At the same time, the (*x*, -*x*) phase modulation of the PMRR sequence and its rotor synchronization are perfectly remained. In dipolar-coupled *I*-*S* spin pair, this echo based on PMRR is highly selective for zeroth-order *I*-*S* dipolar Hamiltonians (I_zS_z), and we would call it dipolar echo.

Importantly, the dipolar echo can compensate the effect from rf inhomogeneity, and suppress the interference from resonance offset. The explanation will be given as follows.

For *I*-*S* spin pair, the Hamiltonians of spin interactions can be simply described as follows:

$$\widehat{\boldsymbol{\mathcal{H}}} = \widehat{\boldsymbol{\mathcal{H}}}_{ext} + \widehat{\boldsymbol{\mathcal{H}}}_{int} \quad (1)$$

where the first and second terms are external and internal spin interactions, respectively. The external spin interactions exist as the nuclear spin interacts with the external static magnetic field along z axis in laboratory frame $\boldsymbol{B_0} = (0,0,B_0)$ and rf field at x axis:

$$\boldsymbol{B_1}(t) = (\omega_1 \cos[\omega_{0,rf}t + \varphi(t)],0,0) \quad (2)$$

The *I* spin interacts with rf field since the $\boldsymbol{B_1}(t)$ carrier frequency $\omega_{0,rf}$ coincides with its Larmor frequency $\boldsymbol{\omega}_{0,I} = \gamma_I \boldsymbol{B}_0$, where the γ_I is gyromagnetic ratio of *I* nucleus. The ω_1 is the amplitude (in rad/s) of rf irradiation, $\omega_1/2\pi = \nu_1$, and $\varphi(t)$ is the phase of rf irradiation. This interaction results in the rotating frame first-order averaged Hamiltonian:

$$\widehat{\boldsymbol{\mathcal{H}}}_1^{rot} = -\gamma_I \left|\hat{\boldsymbol{I}} \cdot \boldsymbol{B}_1(t)\right| = -\gamma_I \omega_1 \hat{I}_x \quad (3)$$

where $\hat{\boldsymbol{I}} = (\hat{I}_x, \hat{I}_y, \hat{I}_z)$. For R^3 experiment using $n = 2$ condition, the rf amplitude is two times of the MAS frequency, $\omega_1 = 2\omega_r$. Apparently, the $\widehat{\boldsymbol{\mathcal{H}}}_1^{rot}$ is time-independent. With the absence of resonance offset and rf mismatch, $\widehat{\boldsymbol{\mathcal{H}}}_1^{rot}$ locks the I spin magnetization at *x* axis. However, in real experiment, multiple *I* spin can exhibit

different chemical shifts. This leads to difference between rf carrier frequency $\omega_{0,rf}$ and the exact resonance frequency of a specific *I* spin, $\omega_{iso,I} = \gamma_I \sigma_{iso} \boldsymbol{B}_0$, where σ_{iso} is the isotropic part of the *I* spin chemical shielding tensor. The Hamiltonian of the *I* spin offset in rotating frame can be written as:

$$\widehat{\boldsymbol{\mathcal{H}}}_{\Omega}^{rot} = -(\omega_{iso,I} - \omega_{0,rf})\hat{I}_z = -\Omega \hat{I}_z \tag{4}$$

Besides, in the rf coil surrounding the sample rotor, the $\boldsymbol{B_1}(t)$ field is usually inhomogeneity.[7] This means that at a specific position in the rotor, the actual rf amplitude $\omega_{1,I}$ experienced *I* spin can be mismatched from ω_1. Therefore, for this *I* spin the Eq.3 should be modified into:

$$\left|\widehat{\boldsymbol{\mathcal{H}}}_{1,I}^{rot}\right| = -\gamma_I \left|\hat{\boldsymbol{I}} \cdot \boldsymbol{B}_{1,I}(t)\right| = -\gamma_I \omega_{1,I} \hat{I}_x \tag{5}$$

Now, applying further frame transformation to $\widehat{\boldsymbol{\mathcal{H}}}_{\Omega}^{rot}$ and $\widehat{\boldsymbol{\mathcal{H}}}_{1,I}^{rot}$ separately, using toggling frame propagator $\hat{U}(t) = e^{-i\widehat{\boldsymbol{\mathcal{H}}}_1^{rot} t}$:

$$\widehat{\boldsymbol{\mathcal{H}}}_{\Omega}^{toggling} = \hat{U}(t)\widehat{\boldsymbol{\mathcal{H}}}_{\Omega}^{rot}\hat{U}^{-1}(t) = -cos\theta \cdot \Omega \hat{I}'_z \tag{6}$$

where $\theta = \arctan(\omega_1/\Omega)$ denotes the angle between the $\boldsymbol{B}_0$ and the effective field to which $\hat{I}'_z$ is parallel. When consider the rf mismatch on *I* spin only, the same frame transformation leads to:

$$\widehat{\boldsymbol{\mathcal{H}}}_{1,I}^{toggling} = \hat{U}(t)\widehat{\boldsymbol{\mathcal{H}}}_{1,I}^{rot}\hat{U}^{-1}(t) = -\gamma_I \Delta\omega_1 \hat{I}'_z \tag{7}$$

where $\Delta\omega_1 = \omega_1 - \omega_{1,I}$ is the rf mismatch on the specific *I* spin.

According to Eq.6, the size of resonance offset Hamiltonian is reduced by cosθ under R^3 irradiation. For dipolar echo based on PMRR sequence (**Figure S2b**), the R^3 irradiation is not interrupted. Therefore, compared to conventional SR4-D-RINEPT where the SR4 recoupling sequence is separated by multiple echo delays, the DEER-INEPT can suppresses the effect from resonance offset through the entire transfer process. Besides, as the rf amplitude ω_1 increased by window modification and the cosθ approaching to zero, the resonance offset Hamiltonian is suppressed more effectively.

As for the effects from rf inhomogeneity, the large rf Hamiltonian $\widehat{\boldsymbol{\mathcal{H}}}_1^{rot}$ is reduced

to a small mismatch term $\widehat{\boldsymbol{\mathcal{H}}}_{1,I}^{toggling}$ in R^3 irradiation. Moreover, different from the simple R^3 irradiation, the dipolar echo maintains the (*x*, -*x*) phase modulation from PMRR. According to Eq. 2, π phase shift in the dipolar echo leads to sign change of the $\boldsymbol{B_1}(t)$ and the resulting mismatch term $\widehat{\boldsymbol{\mathcal{H}}}_{1,I}^{toggling}$. This rf mismatch occurs in macroscopic scale, varying smoothly over the entire sample volume, while the recoupled *I*-*S* dipolar Hamiltonians $\widehat{\boldsymbol{\mathcal{H}}}_{IS}^{toggling}$ is microscopic (within 1 nm). Thus, the two Hamiltonians, $\widehat{\boldsymbol{\mathcal{H}}}_{1,I}^{toggling}$ and $\widehat{\boldsymbol{\mathcal{H}}}_{IS}^{toggling}$, can be assumed to be commutative with each other, i.e., $[\widehat{\boldsymbol{\mathcal{H}}}_{1,I}^{toggling}, \widehat{\boldsymbol{\mathcal{H}}}_{IS}^{toggling}] \approx 0$. As consequences, (*x*, -*x*) phase modulation in dipolar echo can cancel the small rf mismatch term by alternatively changing the sign of $\widehat{\boldsymbol{\mathcal{H}}}_{1,I}^{toggling}$, without significantly effecting the recoupling dipolar term $\widehat{\boldsymbol{\mathcal{H}}}_{IS}^{toggling}$. As the rf mismatch at specific rotor position cancelled out, the DEER-INEPT is thus insensitive to rf inhomogeneity.

1.2 Explanations of DEER-INEPT pulse sequence

The DEER-INEPT has similar mechanism for heteronuclear polarization transfer as the present RINEPT methods[8,9]. **Figure S2c** provides a simple illustration for the involved spin states in the polarization transfer. In dipolar-based RINEPT (D-RINEPT), the coupled state of *I*-*S* spin pair is reintroduced by zero-quantum (ZQ) heteronuclear dipolar recoupling sequences, such as REDOR,[1,10] R^3,[11] SR4,[9,12] $R12_3^5$,[13,14] and PMRR[6]. The recoupling seqeunces, in conventional D-RINEPT, are seperated by echo delayes for rotor synchronization. While in DEER-INEPT, no echo delay is required due to the application of the two dipolar echoes. Therefore, the dipolar recoupling is continuous during the entire polarization trasnfer process as indicated by the dashed squares in **Figure S2d**. This continuity of the PMRR sqeunce in DEER-INEPT means that the π/2 pulses between two dipolar echoes, as indicated by black trangles in **Figure S2d**, use the same rf amplitude as the PMRR seqeunce. If these π/2 pulses use different rf amplitude, the mismatched rf strength during polarization trasnfer will lower the

efficiency of DEER-INEPT. Note, in conventional D-RINEPT, replacing recoupling sequences from SR4 to PMRR indeed can cause difeerent performance, as shown in **Figure S2**, but the discrepency is much less significant compared to DEER-INEPT. Clearly, the dipolar echo design dominates the improvement of DEEr-INEPT over SR4-D-RINEPT.

Apart from the improvement in robustness, the dipolar echoes in DEER-INEPT also allow polarization transfer in short recoupling time, which can be important for short range transfer between strongly coupled spins like bonded ^{1}H-^{17}O. Comparison between **Figure 2b** and **Figure 2c** clearly shows the compactness of DEET-INEPT over the conventional SR4-D-RINEPT. For the shortest possible recoupling time, the DEER-INEPT requires 4 rotor cycles ($4\tau_r$, as shown in **Figure 1b** and **Figure S2d**). However, the SR4-D-RINEPT, even with SR4 sequence using the shortest two-step supercycle instead of the normal three steps[15], requires at least 16 rotor cycles where 8 rotor cycles are used for dipolar recoupling and other 8 rotor cycles are occupied by echo delays. This doubled recoupling time makes SR4-D-RINEPT more susceptive to T_2 relaxation. It is possible to use 4 rotor cycles as total recoupling time in SR4-D-RINEPT, at the expanse of using $R4_1^2$ for heteronuclear dipolar recoupling.[12] On one hand, the $R4_1^2$ sequence also introduces homonuclear dipolar interactions that hampers the transfer efficiency. On the other hand, 8 rotor cycles are still required by echo delays, making the total (shortest possible) duration for SR4-D-RINEPT polarization transfer is 12 rotor cycles. Whereas in the DEER-INEPT using the shortest recoupling time of $4\tau_r$, the PMRR still has complete (x, -x) phase modulation in each dipolar echo (**Figure S2d**), leading to more effective suppression for homonuclear dipolar coupling. In short, without echo delay, the total duration of DEER-INEPT polarization transfer always equals the dipolar recoupling time, making the method more effective in probing short range atomic correlation and less affected by T_2 relaxation.

As the recoupling time increased, the phase cycling of PMRR sequence in DEER-INEPT is more complicate than SR4-D-RINEPT. The latter increases the recoupling time by simply adding the SR4 unit (usually $[R4_1^2R4_1^{-2}]$ spanning two rotor cycles, or

$[R4_1^2]_0[R4_1^2]_{120}[R4_1^2]_{240}$ spinning three rotor cycles), leading to increment of $8\tau_r$. While the DEER-INEPT, with increment of $4\tau_r$, increases the recoupling by adding half of the PMRR unit, $[\pi_x\pi_x\pi_x\pi_x]$ or $[\pi_{-x}\pi_{-x}\pi_{-x}\pi_{-x}]$ both spanning one rotor cycle. As consequences, DEER-INEPT can use two types of PMRR phase cycle, as indicated by scheme **1** and scheme **2** in **Figure S2d**. Both schemes maintain the (x, -x) phase modulation of PMRR sequence through the entire polarization transfer process. The attached pulse program in this supporting information uses the phase cycle of scheme **1**.

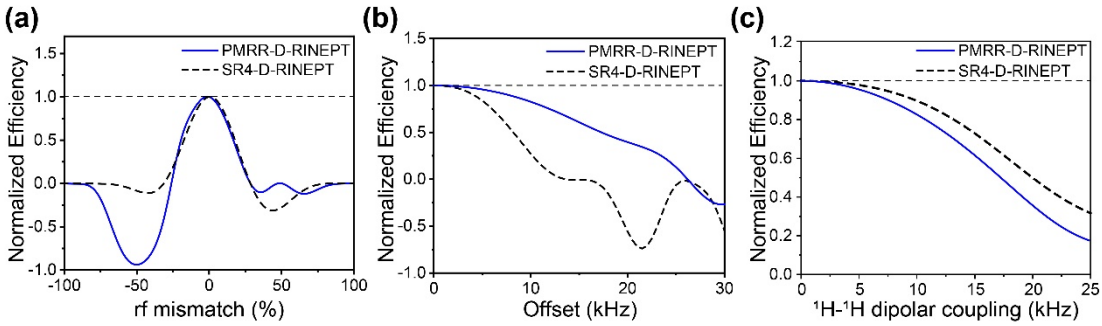

Figure S3. Simulated robustness of $^{1}H \rightarrow ^{15}N$ PMRR-D-RINEPT (solid blue lines) and SR4-D-RINEPT (dashed black lines) under the interferences of (a) rf mismatch, (b) resonance offset and (c) ^{1}H-^{1}H dipolar coupling. The PMRR-D-RINEPT uses the same pulse sequence (**Figure 2c**) as SR4-D-RINEPT, but the SR4 sequence is replaced by windowless PMRR sequence. The simulations use 18.8 T magnetic field, with 60 kHz MAS for (a) and (b), 20 kHz MAS for (c).

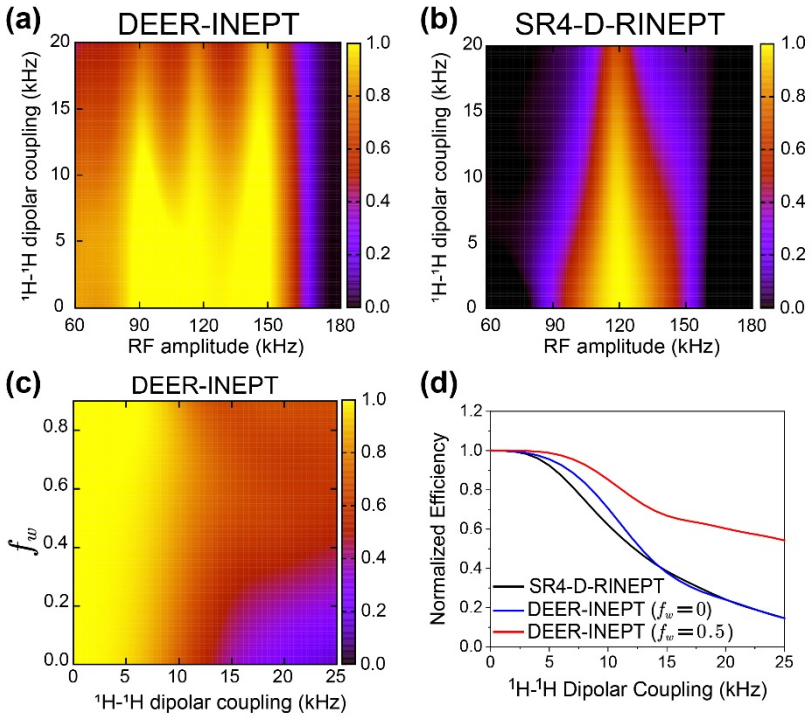

Figure S4. Simulations of transfer efficiency of (a) DEER-INEPT ($f_w = 0$) and (b) SR4-D-RINEPT in tetrahedral $^{15}N^1H_4$ spin system, under the interferences of ^{1}H-^{1}H dipolar coupling and RF mismatch, in 60 kHz MAS. (c) The transfer efficiency of DEER-INEPT under the interferences of ^{1}H-^{1}H dipolar coupling with various f_w. (d) Comparisons of the robustness of DEER-INEPT and SR4-D-RINEPT with different ^{1}H-^{1}H dipolar couplings. The magnetic field in simulations is 18.8 T, and the spinning frequency is 60 kHz. More details for the simulation parameters are included in **Simulations and Experiments**.

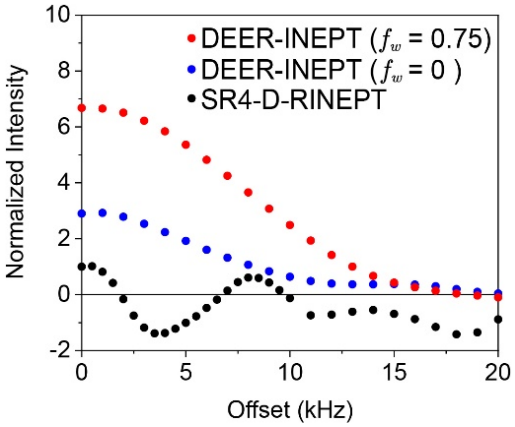

Figure S5. In ADP and 10 kHz MAS, the $^{1}H \rightarrow ^{31}P$ transfer efficiency of DEER-INEPT and SR4-D-RINEPT with increasing ^{1}H offset. The magnetic field in simulations is 9.4 T. More experimental details are included in **Simulations and Experiments**.

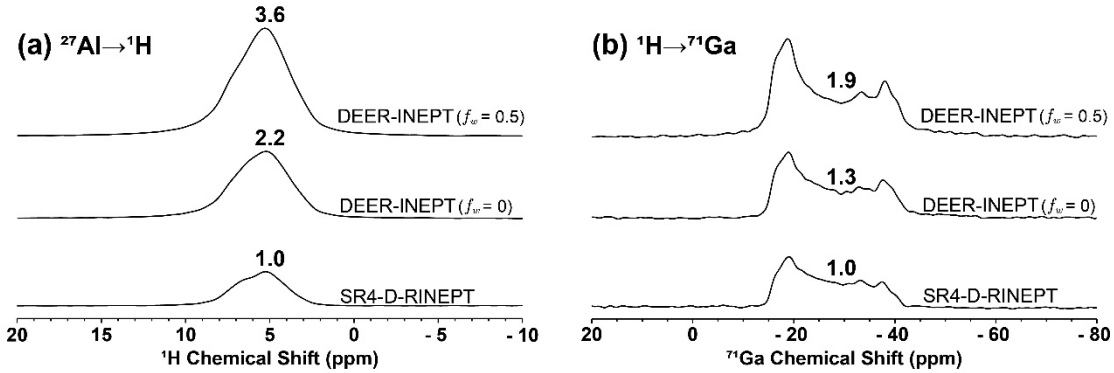

Figure S6. Comparisons of the polarization transfer efficiencies between DEER-INEPT and SR4-D-RINEPT in (a) $^{27}Al \rightarrow {}^{1}H$ transfer in γ-Al_2O_3 and (b) $^{1}H \rightarrow {}^{71}Ga$ transfer in $Ga(acac)_3$. The experiments are operated in 18.8 T magnet, using 20 kHz spinning frequency. The total signal areas of each spectrum, compared with the signal areas from SR4-D-RINEPT, are indicated on top of each spectrum.

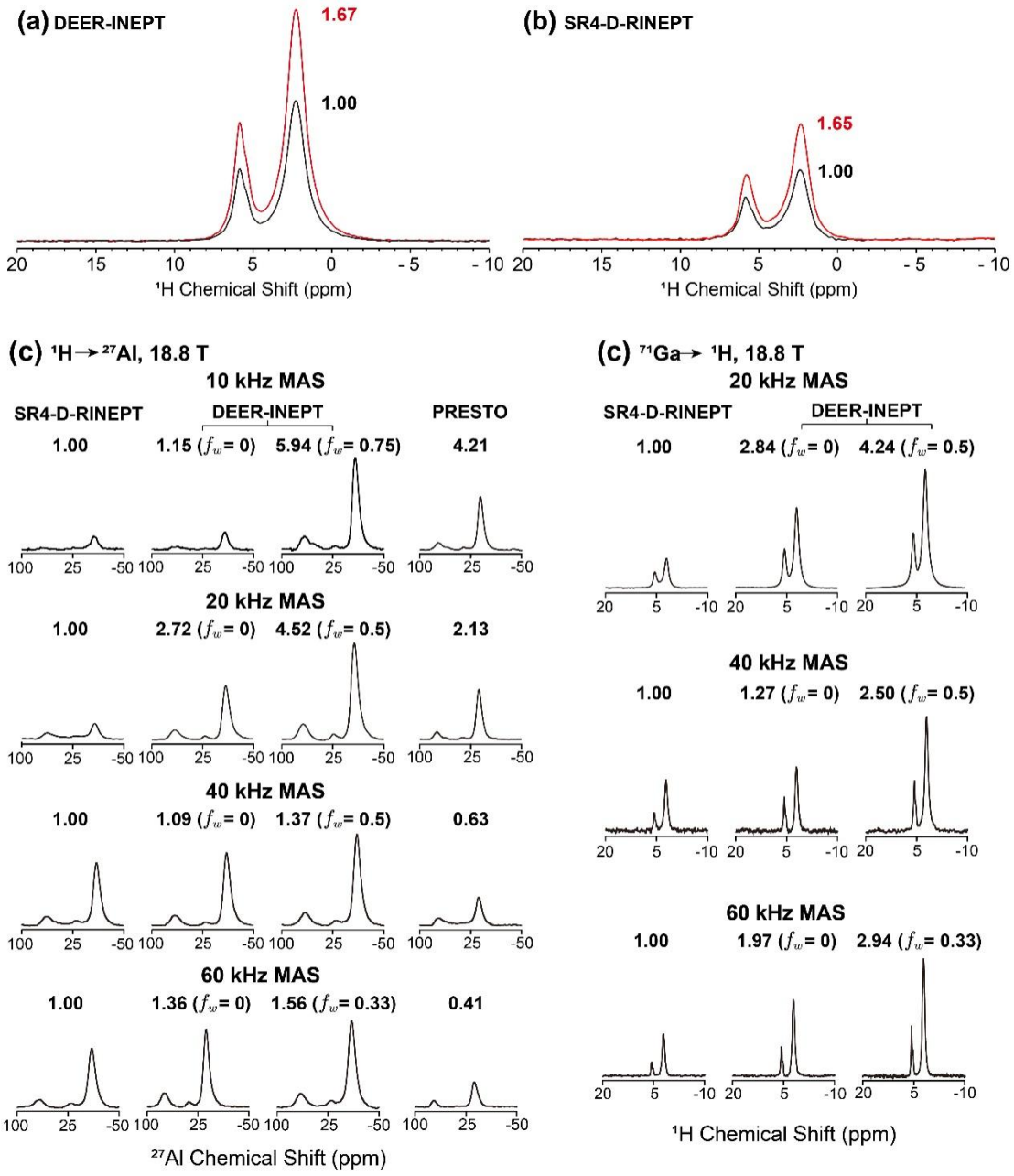

Figure S7. Experimental spectra of γ-Al_2O_3 and $Ga(acac)_3$. Enhancement factors from saturation of ^{71}Ga satellite transition in (a) ^{71}Ga → ^{1}H DEER-INEPT ($f_w = 0$) and (b) ^{71}Ga → ^{1}H SR4-D-RINEPT. The experiments are operated in 18.8 T magnet and 20 kHz MAS. The spectra with and without WURST saturation of ^{71}Ga satellite transition are presented in red and black lines, respectively. (c) ^{27}Al spectra from ^{1}H→^{27}Al polarization transfer. (d) ^{71}Ga spectra from ^{71}Ga→^{1}H polarization transfer. The methods and MAS conditions are illustrated in the spectra. Experimental details are included in **Simulations and Experiments**.

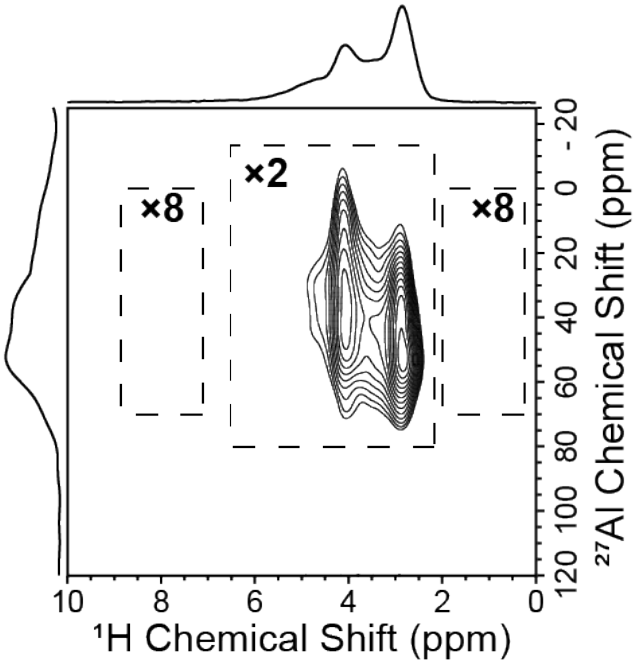

Figure S8. 2D ^{1}H-{^{27}Al} SR4-D-HMQC spectra of dehydrated HY zeolite. The details of the experiments are summarized in **Simulation and Experiments**.

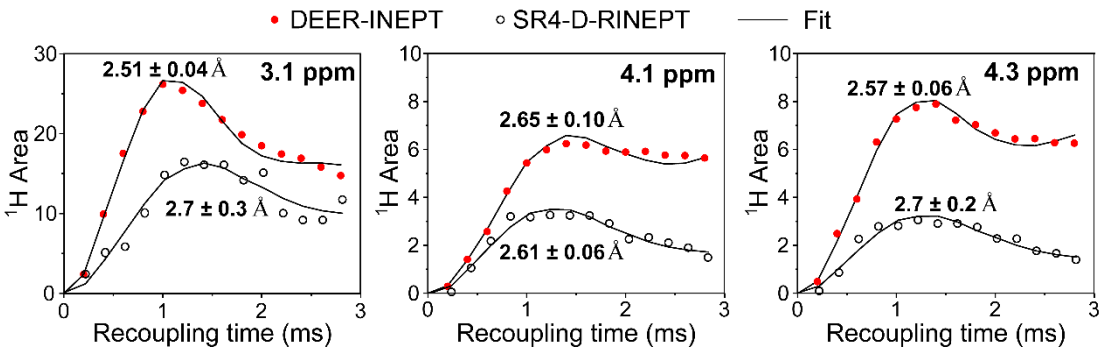

Figure S9. Experiments and fitting of the buildup curves from ^{27}Al→^{1}H DEER-INEPT (red dots) and SR$-D-RINEPT (black circles).

1. Experimental Parameters

1.1 γ-alumina

All experiments of γ-alumina were operated in 18.8 T AV NEO Bruker NMR spectrometer. The experimental parameters from 10 kHz to 60 kHz are listed in **Table S1**.

Table S1. Parameters of experiments in γ-alumina

10 kHz MAS (3.2 HX probe)							
Methods		^{1}H pulses /kHz		^{27}Al pulses /kHz		$\nu_{1,rec}$ /kHz	τ_{rec} /ms	Recycle delay /s
		π/2	π	π/2	π			
SR4-D-RINEPT		56.2				20	0.8	0.5
DEER-INEPT	$f_w = 0$	56.2	-	35.7		20	0.8	
	$f_w = 0.75$		-			80	0.4	
$R18_1^7$-PRESTO		-	-			90	0.4	
20 kHz MAS (3.2 HX probe)							
Methods		^{1}H pulses /kHz		^{27}Al pulses /kHz		$\nu_{1,rec}$ /kHz	τ_{rec} /ms	Recycle delay /s
		π/2	π	π/2	π			
SR4-D-RINEPT		65.8				40	0.8	1.5
DEER-INEPT	$f_w = 0$	65.8	-	50		40	0.8	
	$f_w = 0.5$		-			80	0.6	
$R18_2^5$-PRESTO		-	-			90	0.8	
40 kHz MAS (1.3 HX probe)							
Methods		^{1}H pulses /kHz		^{27}Al pulses /kHz		$\nu_{1,rec}$ /kHz	τ_{rec} /ms	Recycle delay /s
		π/2	π	π/2	π			
SR4-D-RINEPT		113.6				80	0.7	0.5
DEER-INEPT	$f_w = 0$	113.6	-	35.7		80	0.7	
	$f_w = 0.5$		-			160	0.6	
$R20_3^4$-PRESTO		-	-			133	0.3	
60 kHz MAS (1.3 HX probe)							
Methods		^{1}H pulses /kHz		^{27}Al pulses /kHz		$\nu_{1,rec}$ /kHz	τ_{rec} /ms	Recycle delay /s
		π/2	π	π/2	π			
SR4-D-RINEPT		113.6				120	0.666	0.5
DEER-INEPT	$f_w = 0$	113.6	-	35.7		120	0.666	
	$f_w = 0.33$		-			180	0.533	
$R16_3^2$-PRESTO		-	-			160	0.4	

1.2 $Ga(acac)_3$

All experiments in $Ga(acac)_3$ were operated in 18.8 T AV NEO Bruker NMR spectrometer. The experimental parameters from 20 kHz to 60 kHz are listed in **Table S2**.

Table S2. Parameters of experiments in $Ga(acac)_3$

20 kHz MAS (3.2 HX probe)						
Methods		^{71}Ga pulses /kHz		$\nu_{1,rec}$ /kHz	τ_{rec} /ms	Recycle delay /s
		π/2	π			
SR4-D-RINEPT		27.78		40	0.8	0.15
DEER-INEPT	$f_w = 0$			40	0.8	
	$f_w = 0.5$			80	0.8	
40 kHz MAS (1.3 HX probe)						
Methods		^{71}Ga pulses /kHz		$\nu_{1,rec}$ /kHz	τ_{rec} /ms	Recycle delay /s
		π/2	π			
SR4-D-RINEPT		50		80	1.2	0.15
DEER-INEPT	$f_w = 0$			80	1.2	
	$f_w = 0.5$			160	1.2	
60 kHz MAS (1.3 HX probe)						
Methods		^{71}Ga pulses /kHz		$\nu_{1,rec}$ /kHz	τ_{rec} /ms	Recycle delay /s
		π/2	π			
SR4-D-RINEPT		50		120	1.133	0.15
DEER-INEPT	$f_w = 0$			120	1.2	
	$f_w = 0.33$			180	1.0	

1.3 HY zeolite

All experiments in HY zeolite were operated in 18.8 T AV NEO Bruker NMR spectrometer. The experimental parameters at 20 kHz are list in **Table S3**.

Table S3. Parameters of experiments in HY zeolite

20 kHz MAS (3.2 HX probe)						
Methods		^{27}Al pulses /kHz		$\nu_{1,rec}$ /kHz	τ_{rec}* /ms	Recycle delay /s
		π/2	π			
SR4-D-RINEPT		27.78		40	0.8	0.15
DEER-INEPT	$f_w = 0$			40	0.8	
	$f_w = 0.5$			80	0.8	
SR4-D-HMQC				40	0.8	0.7

* In the experiments of producing ^{1}H buildup curves from ^{27}Al→^{1}H transfer, the τ_{rec} is varied from 0.2 to 2.8 ms.

2. Pulse Program of the DEER-INEPT method

```
;DEER-INEPT using PMRR for heteronuclear dipolar recoupling
;
;Written by Lixin Liang 05.15.2020, contact llx_dicp@dicp.ac.cn
;
;Avance III version
;parameters:
;p3 : Proton 90 deg pulse (pl12) for excitation
;p4 : 180 deg pulse (pl2) in PMRR, must < 0.25*rotor_period
;p5 : 90 deg pulse in PMRR
;p1 : X 90 deg pulse (pl1)
;p20 : Pulse for f1 presat (plw15)
;pl1 : Power level for selective X 90 deg pulse
;pl2 : PMRR high power recoupling, must > 2*spinning_frequency
;
##########################################################
;    ##### Further optimization of pl2 is recommended for maximizing signal intensity. #####
;
##########################################################
;pl12 : H90 & decoupling power level (if not PLW13)
;pl13 : special decoupling power level
;cnst21 : on resonance, usually = 0
;cpdprg2 : e.g. cw, spinal64 (at PLW12)
;d1 : recycle delay
;d10 : echo delay d10 in X chennel
;d11 : echo delay d11 in X chennel
;d12 : echo delay d12 in X chennel
;l0 :loop couneter for PMRR, Recoupling time = 4tr*l0
;l12 : = l0 - 2, = 1,5,9,...for complete cycle
;pcpd2 : pulse length in decoupling sequence
;
;
;$CLASS = Solids
;$DIM = 2D
;$TYPE = H -> X    dipolar-based INEPT
;$SUBTYPE = simple 1D
;$COMMENT = DEER-INEPT using PMRR for heteronuclear dipolar recoupling
;
;


prosol relations=<solids_cp>

#include <Avancesolids.incl>

;"l0 = 0"
"p2 = p1*2"
;"p4 = p3*2"
"p5 = p4/2"
;"d3 = 1s/cnst31 - p2/2"
;"d4 = 1s/cnst31-p2/2-p1/2"
"d10 = l0*1s/cnst31 - p2/2"
"d11 = l0*1s/cnst31 - p2/2 - p1/2"
"d12 = l0*1s/cnst31 - p2/2 - de"

"d0 = 0"
"in0 = inf1"
"l12 = 4*l0 - 1"

define delay window
"window = 0.25s/cnst31 - p4"
define delay delt180
"delt180 = p4"
define delay delt90
"delt90 = p3"
define delay delt45
"delt45 = p3/2"
define loopcounter ph_pointer
"ph_pointer = 7 - l12%8"

1 ze

2 10m

   d1 do:f2
#ifdef PRESAT1
30 d20
   (p21 pl21 ph0):f1
   lo to 30 times l20
```

```
#endif

   10u

   "ph_pointer = 7 - l12%8"

10    1u ipp13 ipp14
   lo to 10 times ph_pointer

   (p3 ph1 pl12):f2
   d0                          ;t1
   exec_on_chan:f2:t1
      delt90
3     window
      (p4 pl2 ph13^):f2
      lo to 3 times l12

      window
      delt180 ;rpp13
      window ipp13

4     (p4 ph13^):f2
      window
      lo to 4 times l12

      delt45
      (p5 ph3):f2
      delt45

5     window
      (p4 ph14^ pl2):f2
      lo to 5 times l12

      window
      delt180

6     window ipp14
      (p4 ph14^):f2
      lo to 6 times l12
   exec_wait

   exec_on_other
      d10 pl1:f1
      (p2 ph4):f1
      d11
      (p1 ph5):f1
      d11
      (p2 ph6):f1
      d12
   exec_wait

      0.05u cpds2:f2
      go=2 ph31
      1m do:f2 mc #0 to 2 F1PH(ip1, id0)
;       exit
HaltAcqu, 1m
exit

ph0= 0
ph1=0
ph3=1 3
ph4=0 0 2 2
ph5=0 0 0 0 1 1 1 1 2 2 2 2 3 3 3 3
ph6=0 0 2 2 1 1 3 3
ph31=0 2 0 2 1 3 1 3 2 0 2 0 3 1 3 1

ph13 = 2 2 2 2 0 0 0 0
ph14 = 2 2 2 2 0 0 0 0
```

References

(1) Gullion, T.; Schaefer, J. Rotational-Echo Double-Resonance NMR. *J. Magn. Reson.* **1989,** *81*, 196.

(2) Gan, Z.; Grant, D. M.; R., E. R. NMR chemical shift anisotropy measurements by RF driven rotary resonance. *Chem. Phys. Lett.* **1996,** *254*, 349.

(3) Gan, Z. Rotary resonance echo double resonance for measuring heteronuclear dipolar coupling under MAS. *J. Magn. Reson.* **2006,** *183* (2), 235.

(4) Levitt, M. H.; Oas, T. G.; Griffin, R. G. Rotary Resonance Recoupling in Heteronuclear Spin Pair Systems. *Isr. J. Chem.* **1988,** *28*, 271.

(5) Oas, T. G.; Griffin, R. G.; Levitt, M. H. Rotary resonance recoupling of dipolar interactions in solid-state nuclear magnetic resonance spectroscopy. *J. Chem. Phys.* **1988,** *89* (2), 692.

(6) Liang, L.; Ji, Y.; Zhao, Z.; Quinn, C. M.; Han, X.; Bao, X.; Polenova, T.; Hou, G. Accurate heteronuclear distance measurements at all magic-angle spinning frequencies in solid-state NMR spectroscopy. *Chem. Sci,* **2021,** *12* (34), 11554.

(7) Nagashima, H.; Trébosc, J.; Lafon, O.; Pourpoint, F.; Paluch, P.; Potrzebowski, M. J.; Amoureux, J.-P. Imaging the spatial distribution of radiofrequency field, sample and temperature in MAS NMR rotor. *Solid State Nucl. Magn. Reson.* **2017,** *87*, 137.

(8) Amoureux, J.-P.; Trébosc, J.; Wiench, J.; Pruski, M. HMQC and refocused-INEPT experiments involving half-integer quadrupolar nuclei in solids. *J. Magn. Reson.* **2007,** *184* (1), 1.

(9) Giovine, R.; Trebosc, J.; Pourpoint, F.; Lafon, O.; Amoureux, J.-P. Magnetization transfer from protons to quadrupolar nuclei in solid-state NMR using PRESTO or dipolar-mediated refocused INEPT methods. *J. Magn. Reson.* **2019,** *299*, 109.

(10) Hing, A. W.; Vega, S.; Schaefer, J. Transferred-Echo Double-Resonance NMR. *J. Magn. Reson.* **1992,** *96*, 205.

(11) Trébosc, J.; Hu, B.; Amoureux, J.-P.; Gan, Z. Through-space R3-HETCOR experiments between spin-1/2 and half-integer quadrupolar nuclei in solid-state NMR. *J. Magn. Reson.* **2007,** *186* (2), 220.

(12) Nagashima, H.; Trébosc, J.; Kon, Y.; Sato, K.; Lafon, O.; Amoureux, J.-P. Observation of low-γ quadrupolar nuclei by surface-enhanced NMR spectroscopy. *J. Am. Chem. Soc.* **2020,** *142* (24), 10659.

(13) Levitt, M. H. In *Encyclopedia in Nuclear Magnetic Resonance*; Grant, D. M.;Harris, R. K., Eds.; Wiley: Chichester, 2002; Vol. 9.

(14) Gómez, J. S.; Rankin, A. G.; Trébosc, J.; Pourpoint, F.; Tsutsumi, Y.; Nagashima, H.; Lafon, O.; Amoureux, J.-P. Improved NMR transfer of magnetization from protons to half-integer spin quadrupolar nuclei at moderate and high MAS frequencies. *Magnetic Resonance Discussions* **2021,** *2021*, 1.

(15) Brinkmann, A.; Kentgens, A. P. Proton-selective 17O-1H distance measurements in fast magic-angle-spinning solid-state NMR spectroscopy for the determination of hydrogen bond lengths. *J. Am. Chem. Soc.* **2006,** *128* (46), 14758.

(16) Bak, M.; Rasmussen, J. T.; Nielsen, N. C. SIMPSON: A General Simulation Program for solid-state NMR Spectroscopy. *J. Magn. Reson.* **2000,** *147* (2), 296.

(17) Lorieau, J.; McDermott, A. E. Order parameters based on (13)C(1)H, (13)C(1)H(2) and

(13)C(1)H(3) heteronuclear dipolar powder patterns: a comparison of MAS-based solid-state NMR sequences. *Magn. Reson. Chem.* **2006,** *44* (3), 334.

(18) Liang, L.; Ji, Y.; Chen, K.; Gao, P.; Zhao, Z.; Hou, G. Solid-State NMR Dipolar and Chemical Shift Anisotropy Recoupling Techniques for Structural and Dynamical Studies in Biological Systems. *Chem. Rev.* **2022,** *122* (10), 9880.

(19) Power, L.; Turner, K.; Moore, F. The crystal and molecular structure of α-glycine by neutron diffraction–a comparison. *Acta Crystallographica Section B: Structural Crystallography and Crystal Chemistry* **1976,** *32* (1), 11.

(20) Juhl, D. W.; Tošner, Z.; Vosegaard, T. In *Annu. Rep. NMR Spectrosc.*; Elsevier, 2020; Vol. 100.

(21) Bak, M.; Nielsen, N. C. REPULSION, a novel approach to efficient powder averaging in solid-state NMR. *J. Magn. Reson.* **1997,** *125* (1), 132.